2018

Upstream Influence of Axisymmetric Bodies on Trailing Line Vortices

Tanya Sarah Johnson
Lehigh University

Upstream Influence of Axisymmetric Bodies on Trailing Line Vortices

by

Tanya S. Johnson

Presented to the Graduate and Research Committee

of Lehigh University

in Candidacy for the Degree of

Master of Science

in

Mechanical Engineering and Mechanics

Lehigh University

December 2017

This thesis is accepted and approved in partial fulfilment of the requirements for the degree of Master of Science in Mechanical Engineering.

_____
Date

_____
Dr. Justin W. Jaworski, Thesis Advisor

_____
Prof. D. Gary Harlow, Chairperson of
Department of Mechanical Engineering and Mechanics

Acknowledgements

First and foremost, I would like to thank my adviser, Professor Justin W. Jaworski, without whom this research would not have been possible. His guidance, support, and patience has been instrumental in the completion of this work and my success at Lehigh.

Valuable insight and help with the research was given by Dr. Daniel Garmann, Dr. Miguel Visbal, and Dr. Caleb Barnes at the Air Force Research Lab, as well as Dr. Donald Rockwell and Greg Fishman at Lehigh University. I would also like to thank Dr. Douglas Smith and the Air Force Office of Scientific Research for their financial support under the FA9550-15-1-0148 grant.

Finally, I would like to thank my parents and my brother, without their endless support none of this would have been possible. I am eternally grateful for all of the guidance and help they have given me over the years as well as for their seemingly endless patience while I have been pursuing my graduate degrees.

Contents

List of Figures

Abstract

In formation flight, the wings of a leader aircraft generate trailing vortices that travel downstream and interact with the wings of a follower aircraft. The pressure field of the follower wing can effect the trajectory and stability of these trailing vortices prior to their direct impingement. This upstream influence is examined here by analytical and numerical means using the boundary layer approximation of the incompressible Navier-Stokes equations. Under these slenderness assumptions, the classical Batchelor q-vortex is evolved over a finite domain with a prescribed axisymmetric background pressure gradient using a Green's function approach. The presented analysis is restricted by the linearity of the boundary approximations and the requirement that the vortex and axisymmetric imposed pressure gradient are aligned. Results are presented for constant and linear pressure gradients, as well as for pressure fields representative of canonical axisymmetric follower bodies. This work may be extended and applied to the stability analysis of streamwise finite-core vortices arising in formation flight.

Chapter 1

Introduction

The interaction between columnar vortices and a surface can be broken into three distinct classes: (1) parallel, (2) normal, and (3) streamwise vortex-body interactions [1]. The interaction of vortices and surfaces (e.g. cylinders, foils, or wings) can lead to unsteady hydrodynamic loading, which can destabilize the vortex. While the dynamics of the parallel and normal vortex-body interactions has been examined in-depth, streamwise vortex-body interactions have received less attention. Streamwise vortex-body interactions are the enabling fluid dynamic phenomenon of formation flight, due to the benefits to aerodynamic performances. If the follower wing is positioned properly in relation to the leader wing, the follower can capture the upwash from the leader's tip vortex system. This upwash can allow for an increased lift and reduced drag, leading to the significant savings in aerodynamic efficiency and fuel burn [2].

The purpose of the present work is to determine the effects of a downstream body on the mechanics of a Batchelor trailing vortex [3]. Downstream, axisymmetric solid bodies are represented as pressure fields in the region immediately upstream of the body that it impinges upon. The present analysis is restricted to changes in the axial direction rather than changes in the radial direction. By making this restriction, the azimuthal and radial velocities are the same as the velocities formulated by Batchelor [3] in order to keep the self-induced pressure field of the vortex constant. The axial velocity is the only changing component of the flow field.

This thesis is structured to first explore previous work that has been done to theoretically, numerically, and experimentally model the evolution of a trailing line vortex in Chapter 2. This is followed by a description of the research problem in Chapter 3 and an in-depth description of the mathematical model used in Chapter 4. Results are presented for verification of various portions of the numerical integration scheme and and modified centerline axial velocity of the vortex due to an imposed pressure field in Chapter 5. Chapter 6 concludes the report with a brief overview of the the report, concluding thoughts, and future expansion of the work. In-depth mathematical analysis of the pressure field induced by the sphere and coordinate system conversions are attached at the end of the report in the specified appendices.

Chapter 2

Literature Review

The literature review is broken down into three sections: (1) an overview of the Batchelor q-vortex solution [3] and the Heaton *et al.* [4] approximation of the solution; (2) a discussion of the swirl parameter found by Leibovich and Stewartson [5]; (3) an overview of Vortex-Body interactions [1]. The vortex-body interactions are discussed for four cases: vortex-ring–wall, vortex–rotor-blade, vortex-fin, and vortex-wing interactions.

2.1 Trailing Line-Vortex

Batchelor's so-called q-vortex solution [3] forms the basis for most analytical and numerical modeling efforts for the trailing vortex. This analysis determined a relationship between the azimuthal and axial components of the velocity via the self-induced pressure field of the vortex. The Batchelor vortex models the steady, trailing-line vortex that is shed from one side of a wing that may have a strong axial excess or deficit near its axis. The fluid flow is assumed to be steady, incompressible, and axisymmetric about the vortex axis. Batchelor used cylindrical coordinates, (r, θ, z), as seen in Fig. 2.1, and boundary layer approximations in order to determine the velocity field of the vortex, $(u_{\mathrm{r}}, u_\theta, u_{\mathrm{z}})$. Batchelor accounts for the viscous effects upon the trailing line-vortex by allowing for a diffusive increase of the vortex radius that is proportional to the square-root of the axial distance, $\sqrt{z}$. Due to the diffusive nature of the vortex, the azimuthal velocity will gradually

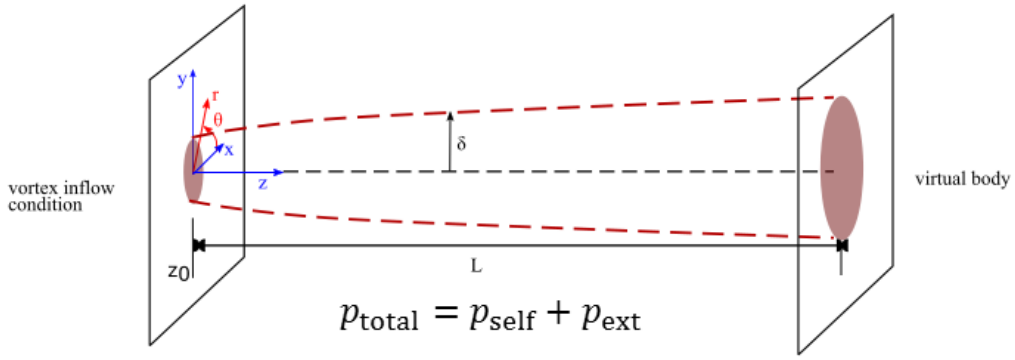

Figure 2.1: Schematic of an axisymmetric, trailing line vortex upstream of an in-line virtual body. Finite-core vortex has a radius, δ, that grows in the downstream direction due to the self-induced and imposed center pressure fields, p_{self} and p_{ext}, respectively. The vortex state is specified at an initial location, z_0, and evolves downstream over a finite distance, L. The global coordinate system is (r, θ, z).

slow down and lead to an increased pressure in the core of the vortex. These effects are accounted for by use of a similarity solution in order to obtain an asymptotic solution for large distances in the axial direction ($z \to \infty$):

$$u_{\text{z}}(r,z) = u_0 - \frac{\Gamma_0^2}{8\nu z}\log\left(\frac{u_0 z}{\nu}\right)e^{-\eta} + \frac{\Gamma_0^2}{8\nu z}\Big[e^{-\eta}\left(\log\eta + ei\left(\eta\right) - 0.807\right) + 2ei\left(\eta\right) - 2ei\left(2\eta\right)\Big] - W\frac{u_0^2}{8\nu z}e^{-\eta}, \tag{2.1}$$

$$u_{\text{r}}(r,z) = 0, \tag{2.2}$$

$$u_\theta(r,z) = \frac{\Gamma_0}{r}\left(1 - e^{-\eta}\right), \tag{2.3}$$

$$\eta = \frac{u_0 r^2}{4\nu z}, \tag{2.4}$$

$$ei(\eta) = \int_\eta^\infty \frac{e^{-\zeta}}{\zeta}\mathrm{d}\zeta. \tag{2.5}$$

The axial velocity component of the Batchelor vortex is generally simplified down to:

$$u_{\text{z}}(r,z) = u_0 - \frac{\Gamma_0^2}{8\nu z}\log\left(\frac{u_0 z}{\nu}\right)e^{-\eta} \tag{2.6}$$

when

$$\frac{\Gamma_0^2}{8\nu z}\left(\log\left(\frac{u_0 z}{\nu}\right) - 0.13\right) + W\frac{u_0^2}{8\nu z} \ll u_0 \tag{2.7}$$

where Γ_0 is the non-zero value of circulation (Γ) that can be determined at large radial distance from the vortex, ν is the kinematic viscosity, u_0 is the free-stream velocity, and W accounts for an initial velocity defect that is induced by the circulation and from the slowing down of the azimuthal velocity due to viscous effects. W can be related to the drag associated with the core of the vortex, D_c:

$$\frac{D_c}{\rho} = -\frac{1}{2}\pi\lambda\Gamma_0^2 + \frac{1}{2}\pi W u_0^2 \tag{2.8}$$

where λ is a positive number far from unity, which allows for (2.1) to be written as:

$$\begin{aligned} u_z = u_0 - \frac{1}{8}e^{-\eta}\left[\frac{2}{\pi}\frac{D_c}{\rho} + \Gamma_0^2\left(\lambda + \log\left(\frac{u_0 z}{\nu}\right)\right)\right] \\ + \frac{\Gamma_0^2}{8\nu z}[e^{-\eta}(\log\eta + ei(\eta) - 0.807) + 2ei(\eta) - 2ei(2\eta)]. \end{aligned} \tag{2.9}$$

Heaton *et al.* [4] simplified the results of Batchelor (2.1)-(2.6) to a two-term asymptotic solution for the axial velocity as $z \to \infty$:

$$\frac{u_z}{u_0} \sim 1 - \alpha(z)e^{-r^2/\delta(z)^2} \tag{2.10}$$

$$\frac{u_r}{u_0} \sim 0 \tag{2.11}$$

$$\frac{u_\theta}{u_0} \sim \frac{\Gamma_0}{r}\left(1 - e^{-r^2/\delta(z)^2}\right) \tag{2.12}$$

$$\alpha(z) = \Gamma_0^2\frac{Re\log(z/Re)}{8z} \tag{2.13}$$

$$\delta(z) = 2\sqrt{z/Re} \tag{2.14}$$

where the Reynolds number is defined using the free-stream velocity and the chord of the wing, C: $Re = u_0 C/\nu$.

2.2 Swirl Parameter and Vortex Stability

A stability criterion for the swirl parameter was developed by Leibovich and Stewartson [5] for the Batchelor vortex. The q parameter is used to define the Batchelor vortex for

numerical and experimental analysis. Barnes *et al.* [6] defines the swirl parameter as:

$$q = \frac{\Gamma}{2\pi r \Delta u} \approx 1.567 \frac{\max\left(\mathrm{u}_\theta\right)}{\Delta u}, \tag{2.15}$$

where Δu is the axial velocity deficit in the vortex core and q can be used to define the velocity flow field of the vortex as shown by Garmann and Visbal [2]:

$$u_\mathrm{r}(r) = 0, \tag{2.16}$$

$$u_\theta(r) = \frac{q\Delta u}{r/r_0}\left(1 - e^{-(r/r_0)^2}\right), \tag{2.17}$$

$$u_\mathrm{z}(r) = 1 - \Delta u e^{-(r/r_0)^2}, \tag{2.18}$$

and r_0 is the initial vortex core radius.

This ratio relates the stability of the vortex to the maximum azimuthal velocity and the maximum axial velocity defect which generally occurs along the centerline of the vortex. q was originally derived by Leibovich and Stewartson [5] as a way to quantify the stability of the vortex. The criterion was derived in order to find a threshold to avoid the amplification of small-wave perturbations in the radial direction. They gave the criterion as:

$$\sigma^2 = \frac{2u_\theta(ru'_\theta - u_\theta)(u_\theta^2/r^2 - u'^2_\theta - u'^2_\mathrm{z})}{(ru_\theta - u_\theta)^2 + (ru)^2} < 0 \tag{2.19}$$

And by substituting the Batchelor velocity field given in (2.2) and (2.6) into (2.19) will yield a stability parameter, $q \geq \sqrt{2}$. When $q \geq \sqrt{2}$ the Batchelor vortex remains stable to small-wave perturbations and when $q < \sqrt{2}$ the vortex is easily destabilized by perturbations in the flow. Thus, by setting q in (2.17) the vortex can be set to a forced initial stability and the stability of the vortex over the course of an experimental or numerical analysis can be found.

2.3 Vortex-Body Interactions

Interaction between streamwise-oriented vortices with downstream bodies (e.g. fins, blades, or wings) are a critical type of flow-structure interaction in both unsteady and steady loading cases. Examples of this interaction include the buffeting of a fin or aircraft tail due to a vortex generated from an upstream body; steady and unsteady loading of rotating blades interacting with a tip-vortex generated from an upstream rotating blade in series; the modification of the lift and drag of a follower wing in formation flight [7]. In the specific case of formation flight, the induced drag on a follower wing can be decreased by an impinging upstream trailing-line vortex being shed from a leader wing, however this can also lead to unintended consequences in the form of unsteady buffeting. This phenomenon has been seen for aircraft and wings of varying sizes, thus it is not restricted to formation flight of large vehicles and can be expanded to micro-air vehicles as shown in work by Kroo [8]. An extensive review of previous work done in the field of vortex-body interactions was performed by Rockwell [1].

This section will discuss the specific interactions between vortex rings and walls as well as the vortex-wing interaction that drives the research discussed in this work. A brief discussion of vortex-fin and vortex-rotor interactions is included.

2.3.1 Vortex-Ring–Wall Interactions

The discussion of vortex-body interactions began with work done by Walker *et al.* [9]. Walker *et al.* worked to further the understanding of the fundamental limitations of inviscid theory upon the ability to model the vortex-ring interactions with a wall. This created a foundation for further theoretical, computational, and experimental works in the field of vortex-body impingement. However, there were limitations to the theoretical analysis done by Walker *et al.* due to it relying heavily upon the initial conditions and circulation results from the experimental analysis. The model that was found by Walker *et al.*, however, only partially describes the results that were seen and the Navier-Stokes analysis that was done by Orlandi and Verzicco [10] allowed for a more accurate solution given that, as briefly

discussed by [9], the boundary layer develops to a chaotic and turbulent state. Due to the turbulence within the boundary layer, it may be prudent to use a more complicated vortex model, such as a hairpin vortex, within the viscous layer near the wall to obtain more accurate results.

Orlandi and Verzicco [10] further expand upon the work done by Walker *et al.* [9] in order to understand the effects of azimuthal instabilities which occur in three-dimensional models and occur due to the interaction of the secondary vortex with the primary vortex. The azimuthal instabilities appear to be associated with the compression of the secondary vortex as it enters the interior of the primary vortex [9–11]. Vortex-rings impacting a flat wall with normal-incidence have been studied in-depth, with more recent work by Cheng *et al.* [11] focusing on vortex-rings impacting at an angle of incidence, θ, between 0 and 40. The effect of θ upon the structure of the vortex is of extreme interest as it can suppress the growth of tertiary rings and introduce a helical instability. Orlandi and Verzicco [10] confirms the results found previously, and have the hallmarks of the axisymmetric case such as (1) vortex stretching, (2) formation of a secondary ring that interacts with the primary, decelerating the radial expansion of the primary ring, (3) the development of azimuthal instabilities, and (4) for sufficiently large values of the Reynolds number, that the interaction between the primary and the secondary vortices results in a tertiary ring being formed.

The work by Cheng *et al.* [11] is in agreement with the experimental results seen by Lin [12]. It is shown that for rings approaching a wall on an angle that an asymmetric shear boundary layer is formed; as the ring is stretched the vorticity of the core increases and a non-uniform vorticity distribution is seen in the core. It should be noted that for small values of θ that the overall vortex structure is not significantly affected. However, for larger values of θ, the secondary ring engulfs the primary ring and a helical structure is developed; the interacting vortices rebound away from the wall which does not allow tertiary rings to develop.

2.3.2 Vortex–Rotor-Blade Interactions

As discussed and sourced in Rockwell [1], the interaction of a streamwise vortex with a blade can lead to unsteady loading of the surface. The streamwise vortex-body interactions have some unifying, identical physical features: (1) displacement of the vortex trajectory in the spanwise direction due to image effects, (2) generation of a separation zone locally on the surface of the blade, and (3) vortex breakdown near the maximum thickness of the blade or directly upstream of the stagnation point. The vortex-blade interaction is confined a fraction of the blade span, which is true for all cases of streamwise vortex-body interaction unlike with parallel vortex-body interactions.

The occurrence of vortex breakdown in these situations is sensitive to the axial pressure gradient, and a complicating factor in the onset of the breakdown is coupled with local modifications of the flow along the surface of the blade. Similarly, the interaction of the vortex with a blade, or wing, is linked to the occurrence of local separation and stall. Wittmer and Devenport [13, 14] and Wittmer *et al.* [15] showed that in the near wake of a blade that rapid changes occur in the structure of the streamwise vortex; the vortex rapidly decays within the wake region as well.

2.3.3 Vortex–Fin Interaction

When a streamwise vortex interacts with a fin, flexible thin plate, or tail, the primary region of interest is between the unsteadiness of the vortex and distribution of loading on the fin [1]. The interaction of the two is complicated, as with the vortex-blade interaction, by the occurrence of vortex breakdown upstream of the leading edge of the plate; unsteady flow phenomenon also plays a role due to the displacement of the core and instabilities arising the breakdown flow field. It has been shown, both experimentally and numerically, that the incident vortex breaks down prior to the leading edge, but that there is a reformation of the vortex on the underside of the wing. This was specifically seen by Patel and Hancock [16] in experiments involving vortex interaction with flat plates and airfoils, as well as in computational work done by Gordnier and Visbal [17].

2.3.4 Vortex–Wing Interactions

Theoretical examination of formation flight using classical aerodynamic theory by Hummel [18, 19] examined the streamwise vortex-wing interaction and found that there are significant benefits to aerodynamics performance. With proper positioning the follower wing is capable of capturing the upwash from the tip vortex shed by the leader wing, which allows for an increase in lift and reduction of the induced drag, leading to energy savings [20]. More recent work done by Ning *et al.* [21] used computational methods to examine the feasibility and benefits of extended formation flight when aircraft are separated by more than ten spans in the streamwise direction. They found that there was significant reduction in drag, but other factors needed to be taken into account specifically wake roll-up, the size of the vortex core, decay of the vortex, as well as gust effects.

Recent work by McKenna and Rockwell [22] and McKenna *et al.* [7] explored experimentally the leader-follower wing interaction and the effect of the impinging vortex upon the downstream body, as well as the effect of the follower wing upon the evolution of the trailing vortex being shed by the leader wing. Similar work has been done performed Garmann and Visbal [2] and Barnes *et al.* [6], as well as previous works cited therein, using high fidelity computations. The series of high fidelity computational studies of streamwise vortices interacting with follower wings has allowed for further insight into the flow physics of the formation flight problem and associated unsteady and steady loading scenarios.

Specifically, the work done by Garmann and Visbal [2] examined the interaction between a streamwise vortex and a wing; this interaction was found to be controlled by the location of the incident vortex in relation to the tip of the follower wing. As the incident vortex moves from outboard to inboard of the wing, the effects upon the tip vortex generated vary significantly and cases of a wing without an impinging vortex were performed and the formation of the tip vortex was seen. However with an outboard positioning of the vortex, a dipole is seen and the tip vortex is enhanced due to mutual induction without a noticeable decay. For the tip-aligned case, both the incident and tip vortices remain distinct; at stations progressing downstream of the wing the structures co-mingle with a

loss of strength and coherency due to their interaction. This co-mingling and mixing of the vortices also appears in ring-wall interactions. Finally, the inboard positioning of the vortex is examined, the incident vortex is bifurcated upon impingement of the wing and the tip vortex is suppressed while the incident vortex is dissipated as it moves downstream from the wing.

Similarly, McKenna *et al.* [7] examined the streamwise vortex-wing interaction experimentally and found similar results. It was found that the vortex-wing interaction is not confined to a region local to the leading edge of the follower wing; there was a region of effect of approximately one chord length upstream of the follower wing and when the trailing vortex was outboard of the follower wing, a region of upstream influence is still detected. The strength of the velocity deficit, $\Delta u = 1 - (u_z/u_0)$, of the vortex is dependent upon the location of impingement and leads to a change in the swirl parameter, q. By examining the swirl parameter, the stability of the vortex can be determined as previously discussed in this work. The swirl parameter allows for an analysis of the stability of the vortex and allows for an examination of instabilities that arise in specific configurations of formation flight, specifically with regards to the sensitivity of the vortex to small-wavelength instabilities. Results from Garmann and Visbal [2,23] shows the growth of an instantaneous helical instability about the exterior of the vortex, which were not easily seen in the experimental work, but the swirl parameter q did fall to a value that would allow for the growth of the instabilities to be seen.

Chapter 3

Problem Statement

The solution of the asymptotic trailing vortex using the analysis of Batchelor [3] with the Green's function approach of Uberoi *et al.* [24] is employed to understand the effect of an external pressure gradients upon the dynamics of the Batchelor q-vortex. The q-vortex was originally derived by Batchelor to approximate a steady, trailing line vortex being shed from a wing and is assumed to be axisymmetric and laminar in nature. In order to approximate this vortex, Batchelor assumed the following:

$$\frac{\partial}{\partial z} \ll \frac{\partial}{\partial r}, \qquad u_{\mathrm{r}} \ll u_{\mathrm{z}}, \qquad |u_{\mathrm{z}} - u_0| \ll u_0, \tag{3.1}$$

which allows for the formulation of governing equations to define the trailing-edge vortex and intrinsically links the axial velocity to the self-induced pressure field of the vortex. The self-induced field is dependent upon changes in the swirl velocity with distance in the axial direction [3].

The assumptions shown in (3.1) allow for the flow region of interest to be restricted to flow fields in which axial gradients are of small magnitude when compared with radial gradients. Similarly, the flow field restricts the motion to the z-direction, which forces the radial velocity to be significantly smaller than the axial velocity. $|u_{\mathrm{z}} - u_0| \ll u_0$ forces the change between the axial velocity and the free-stream velocity to be sufficiently small so that there is an axial velocity deceleration in the core of the fluid [3].

The boundary-layer form of the Navier-Stokes equations in the z-direction equation can be simplified to an approximate form of a cylinder heat conduction equation which was solved by Uberoi *et al.* [24] using analytic Green's function techniques. This solution technique is the basis for examining the impact of external pressure fields upon the axial velocity with a specific focus on the centerline velocity defect and the radial velocity defect. First the effects of constant and linear pressure gradients are examined followed by the effect of a q-vortex impinging upon an in-line, downstream sphere. A schematic of q-vortex interacting with an in-line, axisymmetric virtual body can be seen in Fig. 2.1.

Chapter 4

Mathematical Model

4.1 Governing Equations

Cylindrical coordinates, (r, θ, z), are employed with the corresponding velocity components, $(u_\mathrm{r}, u_\theta, u_\mathrm{z})$. The interaction of a q-vortex with a downstream body can be described by use of the axisymmetric, incompressible, steady-state forms of the Navier-Stokes equations as seen in (4.1) - (4.5).

$$\frac{1}{r}\frac{\partial}{\partial r}(ru_\mathrm{r}) + \frac{\partial u_\mathrm{z}}{\partial z} = 0 \tag{4.1}$$

$$u_\mathrm{z}\frac{\partial u_\mathrm{z}}{\partial z} + u_\mathrm{r}\frac{\partial u_\mathrm{z}}{\partial r} = -\frac{1}{\rho}\frac{\partial p}{\partial z} + \nu\nabla^2 u_\mathrm{z} \tag{4.2}$$

$$u_\mathrm{z}\frac{\partial u_\mathrm{r}}{\partial z} + u_\mathrm{r}\frac{\partial u_\mathrm{r}}{\partial r} - \frac{u_\theta^2}{r} = -\frac{1}{\rho}\frac{\partial p}{\partial r} + \nu\left(\nabla^2 u_\mathrm{r} - \frac{u_\mathrm{r}}{r^2}\right) \tag{4.3}$$

$$u_\mathrm{z}\frac{\partial u_\theta}{\partial z} + u_\mathrm{r}\frac{\partial u_\theta}{\partial r} + \frac{u_\theta u_\mathrm{r}}{r} = \nu\left(\nabla^2 u_\theta - \frac{u_\theta}{r^2}\right) \tag{4.4}$$

$$\nabla^2 = \frac{\partial^2}{\partial r^2} + \frac{1}{r}\frac{\partial}{\partial r} + \frac{\partial^2}{\partial z^2} \tag{4.5}$$

As described in Batchelor's work [3], the flow field of interest can be approximated using boundary-layer type approximations. The boundary-layer formulation assumes that the axial gradients in the flow are small related to radial gradients, and the radial velocity is small when compared to the axial velocity. Similarly, when comparing the axial velocity of the vortex to the free-stream, axial velocity the difference between the two is a sufficiently

small as discussed in Chapter 3 and shown in (3.1).

Employing the governing Navier-Stokes equations and the Boundary Layer assumptions formulated by Batchelor [3], the flow field of interest is described by the linear Boundary Layer equations for an axisymmetric, steady-state trailing-edge line vortex. The governing equations are shown in (4.6)-(4.8).

$$u_0 \frac{\partial u_z}{\partial z} = -\frac{1}{\rho}\frac{\partial p}{\partial z} + \nu\left(\frac{\partial^2 u_z}{\partial r^2} + \frac{1}{r}\frac{\partial u_z}{\partial r}\right) \tag{4.6}$$

$$\frac{u_\theta^2}{r} = \frac{1}{\rho}\frac{\partial p}{\partial r} \tag{4.7}$$

$$u_0 \frac{\partial u_\theta}{\partial z} = \nu\left(\frac{\partial^2 u_\theta}{\partial r^2} + \frac{1}{r}\frac{\partial u_\theta}{\partial r} - \frac{u_\theta}{r^2}\right) \tag{4.8}$$

4.2 Axial Velocity Formulation

Equation (4.8) governs the θ-direction velocity, u_θ, and can be simplified by use of the relationship between the circulation of the flow and the θ-direction velocity: $\Gamma = ru_\theta$. Substituting it into (4.8) and simplifying, the θ-direction vortex equation can be likened to viscous decay of circulation in two-dimensional motion. Utilizing a similarity variable, η, and known asymptotic solutions of the equation form the azimuthal velocity as $z \to \infty$ can be written as:

$$u_\theta = \frac{\Gamma_0}{2\pi r}\left(1 - e^{-\eta}\right), \tag{4.9}$$

$$\eta = \frac{u_0 r^2}{4\nu z}, \tag{4.10}$$

where Γ_0 is the free-stream circulation of the fluid.

From (4.9), Batchelor [3] determined the self-induced pressure of the vortex, shown in (4.12). However, a total pressure field must be found to examine in order to examine the effect of an external pressure field upon the vortex. The pressure of the system, p_{total}, was assumed to be a linear combination of the self-induced pressure field, p_{self}, as well as an external pressure field, p_{ext}. The equation for the total pressure field for the system is shown in (4.13). The axial pressure gradient found by Batchelor [3] and confirmed by

Uberoi *et al.* [24] and is shown in (4.14).

$$\frac{p - p_0}{\rho} = \int_r^\infty \frac{u_\theta^2}{r} dr \tag{4.11}$$

$$p_{\text{self}}(\eta) = \int_\eta^\infty \frac{(1 - e^{-\zeta})^2}{\zeta^2} dx = \frac{(1 - e^{-\eta})^2}{\eta} + 2ei(\eta) - 2ei(2\eta) \tag{4.12}$$

$$p_{\text{total}}(r, \theta, z) = p_{\text{self}}(\eta) + p_{\text{ext}}(r, \theta, z) \tag{4.13}$$

$$\frac{1}{\rho}\frac{\partial p_{\text{self}}}{\partial z} = \left(\frac{\Gamma_0}{2\pi}\right)^2 \frac{u_0}{8\nu z^2}(p_{\text{self}}\eta)' \tag{4.14}$$

In order to determine the axial component velocity, the z-direction boundary layer equation needs to be arranged to a form that is analogous to the transient, one-dimensional heat conduction equation:

$$u_0 \frac{\partial u_{\text{z}}}{\partial z} - \nu \left(\frac{\partial^2 u_{\text{z}}}{\partial r^2} + \frac{1}{r}\frac{\partial u_{\text{z}}}{\partial r} \right) = -\frac{1}{\rho}\frac{\partial p_{\text{total}}}{\partial z}. \tag{4.15}$$

The axial component of the velocity can be found by using the re-arranged form of the linearized z-direction equation of motion, (4.15). Utilizing the Green's function technique demonstrated by Luikov [25] and implemented by Uberoi *et al.* [24]. The axial velocity, u_{z}, was found by treating the axial pressure gradient, $\partial p_{\text{total}}/\partial z$, as a source term of the equation. By doing so, an equation for the axial velocity, $u_{\text{z,p}}$ as a function of the total pressure was found:

$$\frac{u_{\text{z,p}}(r, z)}{u_0} = -\frac{1}{64\pi^2}\left(\frac{\Gamma_0}{\nu}\right)^2 \int_{t_0}^t \int_0^\infty \frac{1}{\rho}\frac{\partial p_{\text{total}}}{\partial t} \frac{e^{-\left(\frac{s^2 + s'^2}{4(t-t')}\right)}}{(t - t')} I_0\left(\frac{ss'}{2(t - t')}\right) s' ds' dt' \ , \tag{4.16}$$

$$s = \frac{u_0 r}{\nu} \ , \tag{4.17}$$

$$t = \frac{u_0 z}{\nu}, \tag{4.18}$$

$$\eta = \frac{s^2}{4t} \ , \tag{4.19}$$

where (s, t) are the non-dimensional radial and axial directions, u_0 is the free-stream axial velocity, and I_0 is the modified Bessel function of the zeroth order.

However, the total axial velocity, u_{z}, is a function of both the pressure term and the

evolution of the vortex inflow condition, $u_z^*(s, t_0)$. The axial velocity as a function of the initial condition, $u_{z,i}$, is shown in (4.20) and the total axial velocity, u_z is shown in (4.22):

$$\frac{u_{z,i}(r,z)}{u_0} = \frac{1}{2}\int_0^\infty u_z^*(s,t_0)\frac{e^{-\left(\frac{s^2+s'^2}{4(t-t_0}\right)})}{t-t_0} I_0\left(\frac{ss'}{2(t-t_0)}\right) s'ds', \tag{4.20}$$

$$t_0 = \frac{u_0 z_0}{\nu}, \tag{4.21}$$

$$u_z(r,z) = u_{z,p}(r,z) + u_{z,i}(r,z), \tag{4.22}$$

where t_0 and z_0 are the non-dimensional and dimensional initial positions of the vortex, respectively.

4.3 Pressure Gradients

The analysis of the effect of an external pressure field upon the dynamics of a q-vortex is performed for three cases: (1) constant background pressure gradient, (2) linear background pressure gradient, and (3) an in-line sphere placed downstream of the vortex. The pressure field for the system is assumed to be a linear combination of the self-induced pressure field, p_{self}, and an external pressure field, p_{ext}, as shown in (4.23). The self-induced pressure field was originally derived by Batchelor and can be seen in (4.12) and the external pressure field derivations are discussed in this section of the work [3].

$$p_{\text{total}}(r,\theta,z) = p_{\text{self}}(\eta) + p_{\text{ext}}(r,\theta,z) \tag{4.23}$$

The total pressure gradient can be converted to non-dimensional form to be substituted into the z-direction BL Navier-Stokes equation:

$$-\left(\frac{\nu}{u_0^2}\right)\frac{\partial p_{\text{total}}}{\partial t} = -\left(\frac{\Gamma_0}{\pi\nu}\right)^2 \frac{u_0}{32}\left[\frac{1}{t^2}\frac{d}{d\eta}(\eta p_{\text{self}}) + \left(\frac{\pi\nu}{\Gamma_0 u_0}\right)^2 \frac{32}{\rho}\frac{\partial p_{\text{ext}}}{\partial t}\right]. \tag{4.24}$$

4.3.1 Constant and Linear Background Pressure Gradients

Two of the special cases examined are for constant and linear axially applied pressure gradients, which disregard any radial effects. The form of the axial pressure gradient is taken to be:

$$\frac{\partial p_{ext}}{\partial z}(r,\theta,z) = \rho(Az + B), \tag{4.25}$$

where A, B are positive constants which are varied for the simulations run. For the constant background pressure gradient, $A = 0$; linear background pressure gradients, $B = 0$.

The expression for the axial pressure gradient in (4.25) can be converted to the non-dimensional coordinate, t:

$$\frac{1}{\rho}\frac{\partial p_{ext}}{\partial t} = \left(\frac{\nu}{u_0}\right)^2 At + \left(\frac{\nu}{u_0}\right) B \tag{4.26}$$

4.3.2 Pressure Gradient Produced by a Sphere

The pressure gradient induced by a sphere was determined by use of potential flow analysis in spherical coordinates and a subsequent transform the local, spherical coordinates of the sphere to the global, cylindrical coordinates of the vortex. The pressure derivation and the coordinate system transformation are detailed in Appendices A and B, respectively. The dimensional form of the axial pressure gradient of a sphere is:

$$\frac{1}{\rho}\frac{\partial p_{\text{ext}}}{\partial z} = 3u_0^2\left(\frac{R_{\text{S}}^3}{z^4} + \frac{R_{\text{S}}^6}{z^7}\right), \tag{4.27}$$

where R_{S} is the radius of the sphere. (4.27) was non-dimensionalized and transformed to the global coordinate system to get the final form of the pressure field:

$$\frac{1}{\rho}\frac{\partial p_{\text{ext}}}{\partial t} = 3u_0^2\left[\frac{I^3}{(t-H)^4} + \frac{I^6}{(t-H)^7}\right], \tag{4.28}$$

$$I = \frac{u_0 R_{\text{S}}}{\nu}, \tag{4.29}$$

$$H = \frac{u_0(z_0 + L + R_{\text{S}})}{\nu}, \tag{4.30}$$

where L is the distance between the initial position of the vortex, z_0, and the front of the sphere.

The numerical calculations were performed for specific ratios of R_s/δ_0. δ_0 is the initial radius of the vortex core and was calculated using (4.31) [4].

$$\delta = \mathrm{f(z)} = \sqrt{\frac{4\nu z}{u_0}}, \qquad \delta_0 = \mathrm{f(z_0)}, \tag{4.31}$$

where z is the axial distance and z_0 is the initial position of the vortex.

4.4 Numerical Simulations

The equations describing the axial velocity cannot be integrated analytically in terms of known functions, thus numerical integration schemes must be employed. The numerical integration code was written in Python script and makes use of built-in SciPy integration schemes. Numerical integration errors occurred due to the divergent nature of the modified Bessel function, I_0, as it diverges to ∞ as $x \to \infty$ causing divergence errors to occur when numerically integrating (4.16) for non-centerline cases, or $r \neq 0$. When $r = 0$, $I_0 = 1$ which avoids the issue. However, in order to avoid problems caused by divergence, the asymptotic form of I_0 for large arguments is utilized. The asymptotic form utilized is from Abramowitz and Stegun [26]:

$$I_0 \sim \frac{e^x}{\sqrt{2\pi x}} + O(x^{-1}), \quad x \to \infty, \tag{4.32}$$

$$x = \frac{ss'}{2(t-t')}, \tag{4.33}$$

the asymptotic form of I_0 is valid as $x \to \infty$, and is not valid for small values of x.

For calculations where $r \neq 0$, the Python script makes use of both the exact and asymptotic forms of I_0. In order to implement this, the code was specifically focused on the value of x and bounding it to an upper limit that would trigger the switch between the exact and asymptotic forms. At each location in the radial direction, x is calculated compared to a maximum value, n, and if $x \geq n$, then (4.32) is utilized. The value of n was

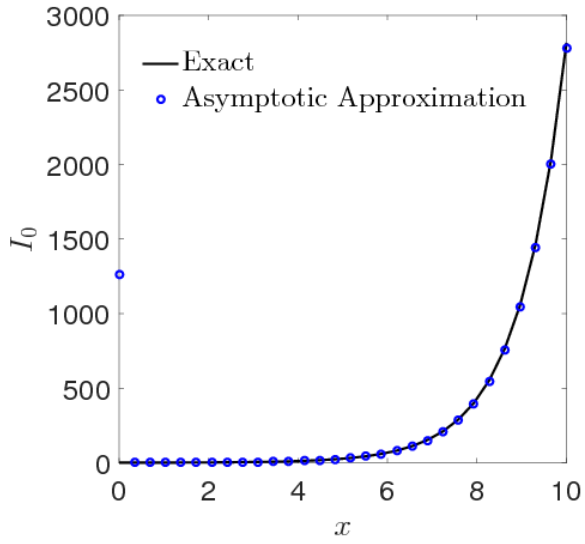

Figure 4.1: Graphical comparison of the accuracy of the first order, asymptotic approximation of the modified Bessel function compared to the Python scripted modified Bessel function.

found through iterative testing of the code and calculations of I_0. A graphical comparison of the accuracy of the asymptotic approximation and the exact, Python scripted I_0 is shown in Fig. 4.1.

Chapter 5

Results

The results presented in this chapter are broken down into two main sections: (1) a discussion of the verification of the code against a corrected version of the results obtained by Uberoi *et al.* [24] and (2) the centerline axial velocity for imposed pressure gradients. Two special cases are presented for the imposed gradient to ensure that the code was functioning in the manner expected; a third case presented is for a pressure field induced by an in-line, axisymmetric sphere.

5.1 Uberoi Results and Verification

In order to ensure that the codes used to calculate the centerline and radial velocity defects were functioning properly, both codes were first run with $p_{\text{ext}} = 0$ to test a purely self-induced case and compare the results found with the results obtained with Uberoi *et al.* [24]. The self-induced pressure was also compared with the results obtained by Batchelor [3] to ensure the proper implementation.

The initial pressure profile found by Batchelor [3] is compared to computational results in Fig. 5.1. The self-induced pressure field of the vortex is seen to decay to zero as η increases. Similarly, the results obtained by Uberoi *et al.* [24] for the pressure derivative is compared to the computational results to ensure the accuracy of the source term for the integration and can be seen in Fig. 5.2.

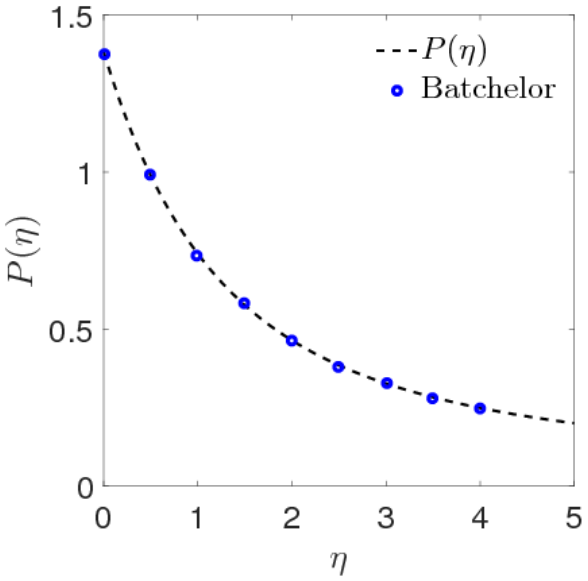

Figure 5.1: Numerical replication of the results obtained by Batchelor [3] for the self-induced pressure field, (4.12), of a trailing edge vortex.

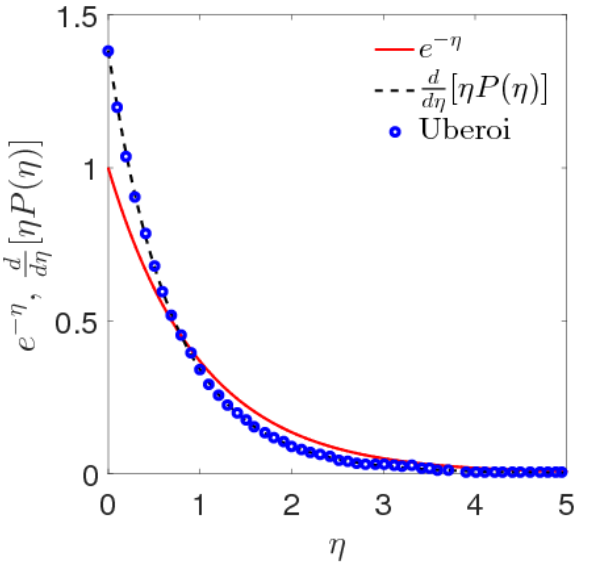

Figure 5.2: Numerical replication of the results obtained by Uberoi *et al.* [24] for the derivative of the self-induced pressure field, (4.14), of a trailing edge vortex.

Of importance, however, is the comparison of the numerical computations of the centerline and radial velocity defects to the results found by Uberoi, et al [24]. The centerline velocity defect for q-vortex is shown in Fig. 5.3. The centerline velocity is shown to begin at the initial prescribed position, $z_0 = 1$m before having a significant spike in axial velocity prior to the velocity decaying. The results of the numerical integration were found to match the results obtained by Uberoi *et al.*, which validated the code.

However, while the results found by Uberoi *et al.* [24] were verified by the code further work done on the problem yielded an issue with the results obtained analytically to results seen in other works that have previously been discussed. The discrepancies were specifically seen in Fig. 5.3, where the results were significantly larger than realistic results that were obtained. The issue was resolved by transforming the upper and lower integration bounds of (4.16) from the dimensional values in z to non-dimensional values in t. Once this modification was made, the results obtained in lieu of the results shown in Fig. 5.3 are more accurate than the results however the results are not comparable to the results that were found by Uberoi *et al.* While the shape remains the same, the magnitude of the velocity is decreased significantly, with the self-induced velocity falling in the range of the free-stream velocity.

Figure 5.4 shows the results of the calculated radial velocity defect at a location of $Z = z/Z_0 = 10$ with the results of Uberoi *et al.* [24] as well as an exponential decay. The results of the calculation match up well with the results obtained by Uberoi *et al.*, and show the exponential decay of the velocity defect as the value of r increases. It should be noted that there is an erroneous point that appears at $\eta \approx 0.025$. It is currently believed that the inaccuracy of this value is due to the changing of the definition of I_0 and is an artifact of the numerical approach taken here.

5.2 Centerline Velocity

The centerline velocity, $u_z(z, 0)$, of the vortex undergoing applied external pressure gradients is shown in Figs. 5.5 and 5.6. The centerline velocity has been non-dimensionalized by

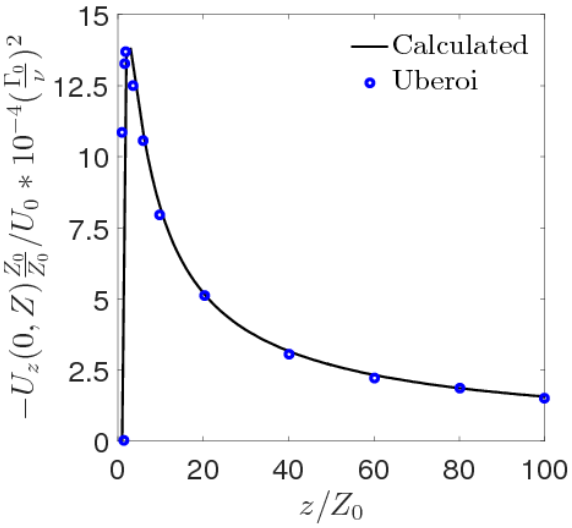

Figure 5.3: Numerical replication of the centerline velocity defect obtained by Uberoi *et al.* [24] for an unmodified q-vortex induced at a location, $z_0 = 1$m with z/Z_0 being the non-dimensional distance downstream.

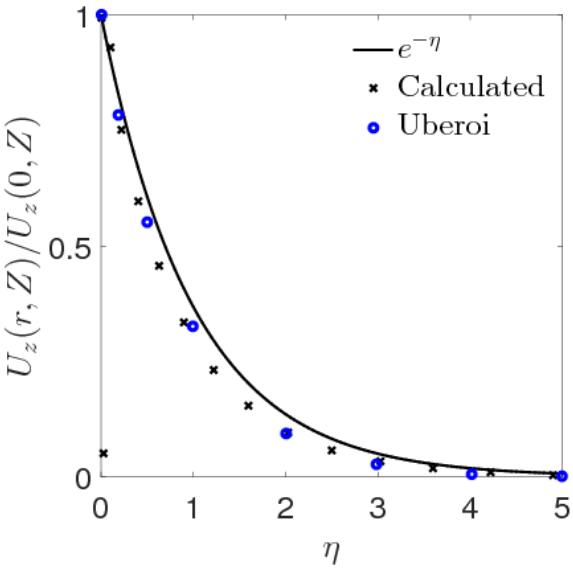

Figure 5.4: Numerical replication of the radial velocity defect obtained by Uberoi *et al.* for an unmodified q-vortex induced at a location $z_0 = 1$m at a fixed axial position, $Z = z/Z_0 = 10$. The similarity variable, η, is proportional to r^2.

the free-stream velocity, u_0, and the axial distance, z, is non-dimensionalized by the initial positions z_0,

$$Z = \frac{z}{z_0}. \tag{5.1}$$

Values for the free-stream velocity, circulation, and chord of the upstream wing were taken by work done by Fishman *et al.* [27] setting the $Re_\Gamma = \Gamma/\nu = 2300$ and $Re_C = u_0 C/\nu = 16000$. For the constant and sphere-induced external pressure gradients the initial position of the vortex is $z_0 = 0.01$m, and has an initial core radius, $\delta_0 = 5.04975\text{x}10^{-4}$m. For the linear external pressure gradient, the initial position of the vortex is $z_0 = 0.1$m, and it has an initial core radius, $\delta_0 = 1.59687\text{x}10^{-3}$m.

The centerline velocity presented in this section is the total axial velocity calculated from the pressure sources in (4.16) and from the evolution of the initial condition in (4.20).

For all of the cases presented the vortex is initialized as a uniform vortex. Due to this assumption the initial centerline velocity of the vortex is forced to: $u_z(r, z_0) = u_0$. Once the vortex is initializes, the centerline velocity begins to decay due to the self-induced pressure field of the vortex. Once the self-induced pressure field decays to zero as shown in Fig. 5.1, the centerline velocity trends back towards u_0. This trend shows that the strength of the vortex is beginning to decay and that the finite-core vortex is beginning to dissipate. If the vortex is initialized differently (e.g. $u_z(r, z_0) \neq u_0$), it may remove the initial period of adjustment from the analysis.

5.2.1 Constant and Linear Background Pressure Gradients

Figure 5.5 shows the results of a constant, applied external pressure gradient (see (4.25)) where B is varied between 0 and 1.0; A is set equal to 0. The initial position of the vortex is $z_0 = 0.01$m and Z is varied between 0 and 10. As B is increased, the axial velocity decreases, however the effects of the external gradient only begins to dominate after the self-induced pressure gradient dies out. The transition between the self-induced pressure dominated regime and the external pressure dominated regimes, this transition occurs at roughly $Z \approx 2$ for all cases. At $Z = 1$, there is a numerical overshoot that exceeds the

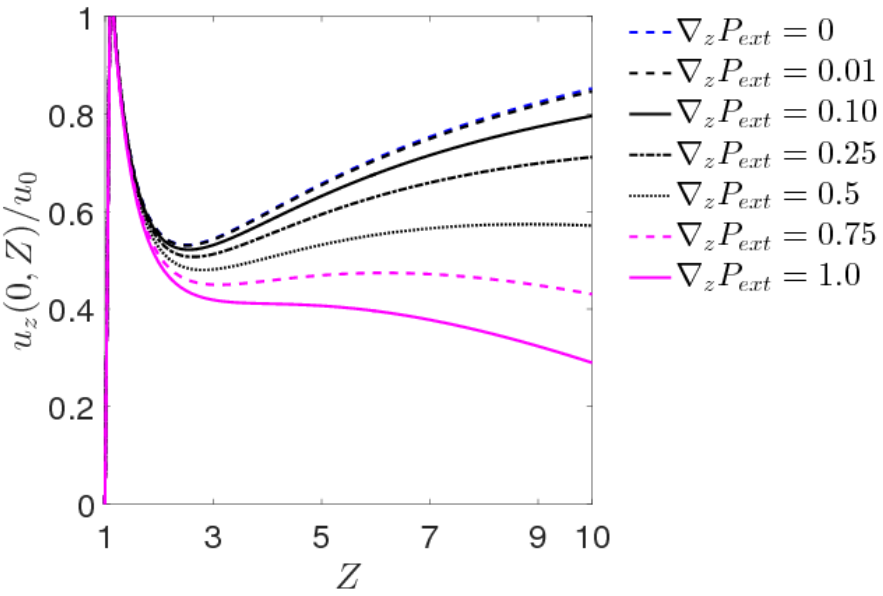

Figure 5.5: Centerline axial velocity of a trailing line vortex of initial radius, δ_0, undergoing an externally applied, constant pressure gradient. The initial position of the vortex is at $z_0 = 0.01$m.

ratio of $u_z(0, Z)/u_0 = 1$ which is due to a numerical integration issues.

Fig. 5.6 shows the results of a linear, applied external pressure gradient where A is varied between 0 and 0.10; B is set equal to 0. Similar to the results seen for the constant linear gradient, there is a region of self-induced pressure domination before transitioning to a region of external pressure gradient domination. The region of self-induced pressure domination is the smallest of the three cases examined in this paper, due to the explicit dependency of the external pressure gradient upon the axial position, or as the distance downstream increases the stronger the externally applied pressure gradient becomes with the strength being dependent upon the value of A. Similarly, the region of effect of the external pressure gradient increases with the value of A; the peak of $u_z(0, Z)/u_0$ decreases slightly with an increase in A.

It should be noted that the self-induced results obtained for the linear gradient differ from the results obtained for both the constant and sphere-induced pressure gradients. This may be due to the initial position used ($z_0 = 0.1$m versus $z_0 = 0.01$m, respectively) or due to a coding error for that specific test case.

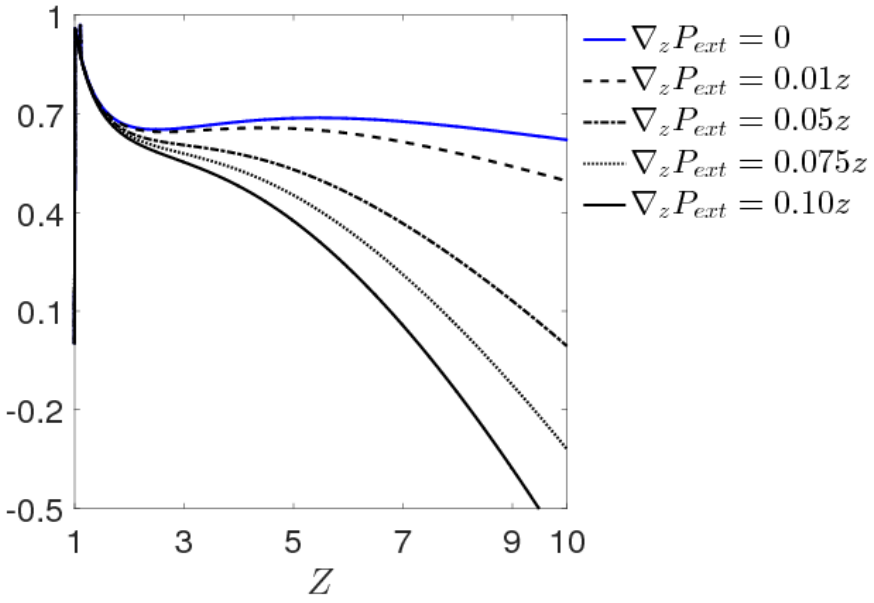

Figure 5.6: Centerline axial velocity of a trailing line vortex of initial radius, δ_0, undergoing an externally applied, linear pressure gradient. The initial position of the vortex is at $z_0 = 0.1$m.

5.2.2 Pressure Gradient Produced by a Sphere

Figure 5.7 shows the effects of an axisymmetric, in-line sphere upon the evolution of the centerline axial velocity, $u_z(0, Z)/u_0$. The presented results are dependent upon the ratio of the sphere radius, R_S to the initial vortex core radius, δ_0. For ratios of $R_S/\delta_0 \leq 1$, the velocity field is insensitive to the presence of the sphere and has the same velocity profile as the self-induced pressure field; as $R_S/\delta_0 \to \infty$ the centerline axial velocity collapses to a single line, with the exception of $Z \approx 10$ which is discussed later in this section. As with the other cases discussed, the flow can be broken up into two regions: (1) a self-induced pressure dominated and (2) sphere pressure dominated regions. The transition between the regions occurs at $Z \approx 5$ for all cases, though as R_S/δ_0 increases the region of sphere pressure domination increases, which is also seen for the other two cases discussed.

The front of the sphere is located at $Z = 10$, so a stagnation point where $u_z(0, Z)/u_0 = 0$ should be occurring at at $Z = 10$. The velocity is not decaying to the proper value, which implies that there is an issue with the analysis in the flow region immediately upstream of the sphere. There may be viscous effects in that region that are not presently being

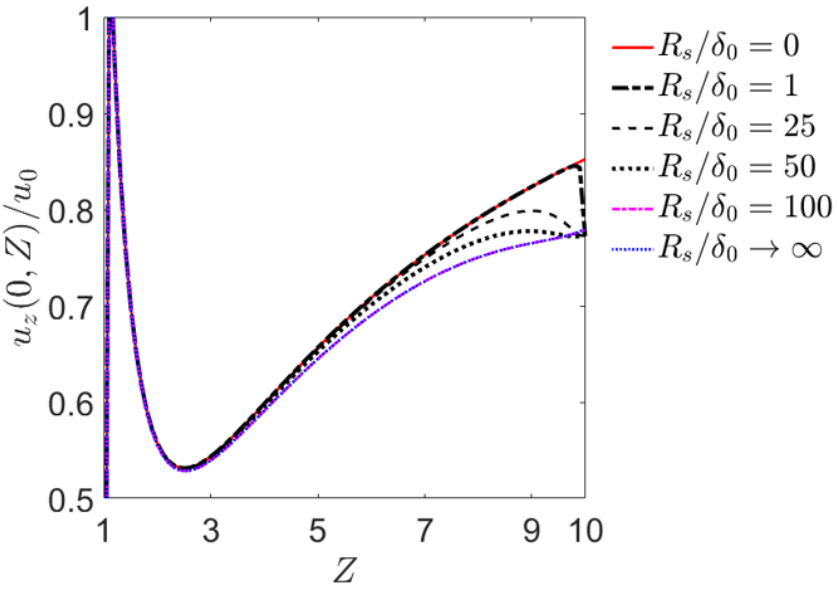

Figure 5.7: Centerline axial velocity of a trailing line vortex of initial radius, δ_0, impinging upon a downstream, in-line sphere of radius, R_S. The initial position of the vortex is at $z_0 = 0.01$m.

accounted for. Further analysis in this region is necessary and will be performed in order to better understand the physics of the region. However, it should be noted that for all of the flows impinging upon a downstream sphere, the velocities do stagnate to a final velocity, $u_z(0, Z)/u_0 \approx 0.75$. The discrepancy may be due to the presence of the evolution of the initial vortex condition as it evolves downstream as it does not decay to zero, but rather has a finite value, whereas the contributions of (4.16) and the pressure terms decays to zero as $Z \to 10$.

Chapter 6

Conclusions and Future Directions

This work studies the effect of applied external pressure gradients upon the evolution of a trailing-line vortex. A review of the current literature and existing theory that models the trailing-line vortex, as well as surveying current work in the field of vortex-body interactions. This thesis lays out a methodology for establishing the base vortex flow from Batchelor [3] and a set of modifications that make it possible to model the effects of external pressure gradients upon the evolution of the axial velocity. The proposed model makes use of Green's functions and allows for the axial velocity of the vortex to be broken down into two components: (1) the velocity due to pressure terms; and (2) the evolution of the axial velocity at the initial position. However, the methodology in this thesis is restricted to axis-aligned axisymmetric solid bodies as well as axial pressure gradients. Any modification in the radial direction will change the base flow and self-induced pressure gradient which invalidates the axisymmetric model. Verifications of the numerical code against the original results found by Uberoi *et al.* [24] were made and new results were presented for three external gradient cases: (1) constant, (2) linear, and (3) sphere-induced pressure gradients.

6.1 Future Work

Future work on this topic will include an analysis of the swirl parameter, q. Determining the appropriate swirl parameter for the problem at hand will allow for the stability of the vortex to be examined and allow for an ease of comparison of the results obtained to current experimental and computational results found in literature. Once the swirl parameter and stability analysis has been performed, the framework laid out in this report will be expanded to non-axisymmetric cases. This expansion will allow for the exploration of effects due to out-of-line, as well as for non-axisymmetric bodies, to be performed.

Bibliography

[1] D. Rockwell. Vortex-body interactions. *Annual Review of Fluid Mechanics*, 30:199 – 229, 1998.

[2] D. J. Garmann and M. R. Visbal. Interactions of a streamwise-oriented vortex with a finite wing. *Journal of Fluid Mechanics*, 767:782 – 810, 2015.

[3] G. K. Batchelor. Axial flow in trailing line vortices. *Journal of Fluid Mechanics*, 20(4):645 – 658, 1964.

[4] C. J. Heaton, J. W. Nichols, and P. J. Schmid. Global linear stability of the non-parallel batchelor vortex. *Journal of Fluid Mechanics*, 629:139 – 160, 2009.

[5] S. Leibovich and K. Stewartson. A sufficient condition for the instability of columnar vortices. *Journal of Fluid Mechanics*, 126:335 – 356, 1983.

[6] C. J. Barnes, M. R. Visbal, and R. E. Gordnier. Analysis of streamwise-oriented vortex interactions for two wings in close proximity. *Physics of Fluids*, page 015103, 2015.

[7] C. McKenna, M. Bross, and D. Rockwell. Structure of a streamwise-oriented vortex incident upon a wing. *Journal of Fluid Mechanics*, 816:306 – 330, 2017.

[8] I. M. Kroo. Innovations in aeronautics. *AIAA Aerospace Sciences Meeting*, pages 2004–001, 2004.

[9] J. D. A. Walker, C. R. Smith, A. W. Cerra, and T. L. Doligalski. The impact of a vortex ring on a wall. *Journal of Fluid Mechanics*, 181:99–140, 1987.

[10] P. Orlandi and R. Verzicco. Vortex rings impinging on walls: axisymmetric and three-dimensional solutions. *Journal of Fluid Mechanics*, 256:615–646, 1993.

[11] M. Cheng, J. Lou, and L. S. Luo. Numerical study of a vortex ring impacting a flat wall. *Journal of Fluid Mechanics*, 660:430–455, 2010.

[12] T. T. Lin. An experimental study of a vortex ring interacting with an inclined wall. *Experiments in Fluids*, 7:453–463, 1989.

[13] K. S. Wittmer and W. J. Devenport. Interaction of a streamwise vortex with a full-span blade. In *Fluid Dynamics Conference*, page 2214, 1994.

[14] K. S. Wittmer and W. J. Devenport. Turbulence structure resulting from a perpendicular airfoil-vortex interaction. *AIAA paper*, pages 96–2014, 1996.

[15] K. S. Wittmer, W. J. Devenport, M. C. Rife, and S. A. Glegg. Perpendicular blade vortex interaction. *AIAA journal*, 33(9), 1995.

[16] M. H. Patel and Q. J. Hancock. Some experimental results of the effect of a streamwise vortex on a two-dimensional wing. *The Aeronautical Journal*, 78(760):151–155, 1974.

[17] R. E. Gordnier and M. R. Visbal. Numerical simulation of the impingement of a streamwise vortex on a plate. *International Journal of Computational Fluid Dynamics*, 12(1):49–66, 1999.

[18] D. Hummel. Aerodynamic aspects of formation flight in birds. *Journal of theoretical biology*, 104(3):321–347, 1983.

[19] D. Hummel. Formation flight as an energy-saving mechanism. *Israel Journal of Zoology*, 41(3):261–278, 1995.

[20] P. B. S. Lissaman and C. A. Shollenberger. Formation flight of birds. *Science*, 168(3934):1003–1005, 1970.

[21] S. A. Ning, T. C. Flanzer, and I. M. Kroo. Aerodynamics performance of extended formation flight. *Journal of Aircraft*, 48(3):855–865, 2011.

[22] C. McKenna and D. Rockwell. Topology of vortex-wing interaction. *Experiments in Fluids*, 57:161, 2016.

[23] D. J. Garmann and M. R. Visbal. Unsteady interactions of wandering streamwise-oriented vortex with a wing. *AIAA Aviation Forum*, pages 2014–2105, 2014.

[24] M. S. Uberoi, B. K. Shivamoggi, and S. S. Chen. Axial flow in trailing line vortices. *Physics of Fluids*, 22(2):214 – 217, 1979.

[25] A. V. Luikov. Analytical heat diffusion. 1968.

[26] M. Abramowitz and I. A. Stegun. Handbook of mathematical functions: with formulas, graphs, and mathematical tables. 1964.

[27] G. Fishman, M. Wolfinger, and D. Rockwell. The structure of a trailing vortex from a perturbed wing. *Journal of Fluid Mechanics*, 824:701 – 721, 2017.

[28] J. D. Anderson Jr. *Fundamentals of aerodynamics*. Tata McGraw-Hill Education, 2010.

Appendix A

Pressure Field Induced by a Sphere

The velocity field produced by a sphere can be considered analytically by utilizing a three-dimensional doublet and superimposing a uniform velocity field with a magnitude, u_0. A diagram of this system is shown in Fig. A.1. Examining this figure the spherical coordinates of the combined free-stream and doublet flow can be written as [28]:

$$u_\kappa = -\left(u_0 - \frac{\mu}{2\pi\kappa^3}\right)\cos\alpha, \tag{A.1}$$

$$u_\alpha = \left(u_0 + \frac{\mu}{2\pi\kappa^3}\right)\sin\alpha, \tag{A.2}$$

$$u_\beta = 0, \tag{A.3}$$

where μ is the strength of the doublet.

Equations (A.1)-(A.3) can be recast in terms of a sphere radius, R_S, by use of the stagnation point at the stagnation velocity: $(u_\kappa, u_\alpha, u_\beta) = (0, 0, 0)$. From (A.2), $u_\alpha = 0$ gives $\sin(\alpha) = 0$, thus the stagnation points are at $\alpha = 0, \pi$. Similarly, (A.1) can be used:

$$u_\kappa = 0 = u_0 - \frac{\mu}{2\pi R_\mathrm{S}^3} \tag{A.4}$$

$$R_\mathrm{S} = \left(\frac{\mu}{2\pi u_0}\right)^{1/3} \tag{A.5}$$

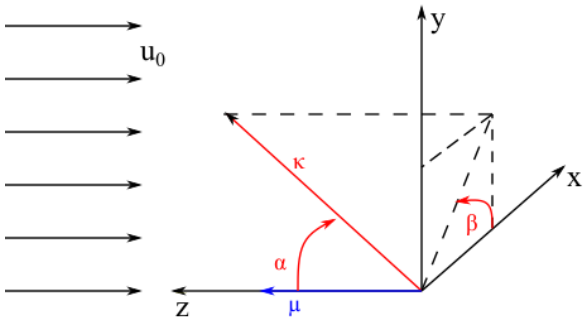

Figure A.1: Superposition of a uniform flow with a three-dimensional doublet.

Inserting the solution from (A.5) into (A.1) and (A.2), the total velocity field for the sphere is found:

$$u_\kappa = -u_0 \left(1 - \frac{R_S^3}{\kappa^3}\right) \cos\alpha, \tag{A.6}$$

$$u_\alpha = u_0 \left(1 + \frac{R_S^3}{\kappa^3}\right) \sin\alpha, \tag{A.7}$$

The region of focus for the problem is along the axial direction, z, so the equations found for the velocity potential can be transformed by setting $\alpha = 0$ and $\beta = 0$, which collapses the κ-direction to the negative z-direction. These assumptions reduces (A.6) and (A.7) to:

$$u_\kappa = -u_0 \left(1 - \frac{R_S^3}{\kappa^3}\right) \tag{A.8}$$

$$u_\alpha = 0 \tag{A.9}$$

Using the final velocity field shown in (A.8) and (A.9), the pressure gradient in the

κ-direction can be found:

$$p_{\text{ext}} = p + \frac{1}{2}\rho\mathbf{V}^2, \tag{A.10}$$

$$\frac{\partial}{\partial\kappa}\left[p_{\text{ext}} = p_s + \frac{1}{2}\rho\mathbf{V}^2\right], \tag{A.11}$$

$$0 = \frac{\mathrm{dp}}{\mathrm{d}\kappa} + \rho\mathbf{V}\frac{\mathrm{d}\mathbf{V}}{\mathrm{d}\kappa}, \tag{A.12}$$

$$\frac{\mathrm{dp}}{\mathrm{d}\kappa} = -\rho\mathbf{V}\frac{\mathrm{d}\mathbf{V}}{\mathrm{d}\kappa}, \tag{A.13}$$

$$\mathbf{V} = u_\kappa\hat{e}_\kappa + u_\alpha\hat{e}_\alpha + u_\beta\hat{e}_\beta, = u_\kappa\hat{e}_\kappa, \tag{A.14}$$

$$\frac{\mathrm{dp}}{\mathrm{d}\kappa} = -\rho\left[-u_0\left(1 - \frac{R_{\mathrm{S}}^3}{\kappa^3}\right)\right]\frac{\mathrm{d}}{\mathrm{d}\kappa}\left[-u_0 + u_0\frac{R_{\mathrm{S}}^3}{\kappa^3}\right], \tag{A.15}$$

$$\frac{\mathrm{dp}}{\mathrm{d}\kappa} = \rho u_0\left(1 - \frac{R_{\mathrm{S}}^3}{\kappa^3}\right)\left[0 + u_0(-3)\frac{R_{\mathrm{S}}^3}{\kappa^4}\right], \tag{A.16}$$

$$\frac{\mathrm{dp}}{\mathrm{d}\kappa} = -3\rho u_0^2\left(\frac{R_{\mathrm{S}}^3}{\kappa^4} - \frac{R_{\mathrm{S}}^6}{\kappa^7}\right). \tag{A.17}$$

In order to transform κ to z, the previous simplifications allows for the κ-direction to be collapsed to the negative Z-direction, or $\kappa = -Z$:

$$\frac{\mathrm{dp}}{\mathrm{d}(-\mathrm{Z})} = -3\rho u_0^2\left(\frac{R_{\mathrm{S}}^3}{(-Z)^4} - \frac{R_{\mathrm{S}}^6}{(-Z)^7}\right), \tag{A.18}$$

$$-\frac{\mathrm{dp}}{\mathrm{dZ}} = -3\rho u_0^2\left(\frac{R_{\mathrm{S}}^3}{Z^4} + \frac{R_{\mathrm{S}}^6}{Z^7}\right), \tag{A.19}$$

$$\frac{\mathrm{dp}}{\mathrm{dZ}} = 3\rho u_0^2\left(\frac{R_{\mathrm{S}}^3}{Z^4} + \frac{R_{\mathrm{S}}^6}{7}\right). \tag{A.20}$$

Therefore the dimensional, axial pressure gradient induced by a sphere that is used to define the total axial pressure gradient is:

$$\frac{1}{\rho}\frac{\partial p_{\text{ext}}}{\partial Z} = 3u_0^2\left(\frac{R_{\mathrm{S}}^3}{Z^4} + \frac{R_{\mathrm{S}}^6}{Z^7}\right), \tag{A.21}$$

where Z is the local axial coordinate for the sphere. Utilizing the transformations in

Appendix B, (A.21) can be transformed to the global coordinate system:

$$\frac{1}{\rho}\frac{\mathrm{dp_{ext}}}{\mathrm{dz}} = 3u_0^2\left(\frac{R_\mathrm{S}^3}{(z-K)^4} + \frac{R_\mathrm{S}^6}{(z-K)^7}\right), \tag{A.22}$$

$$K = z_0 + L + R_\mathrm{S}, \tag{A.23}$$

where z_0 is the initial position of the vortex and L is the finite distance between the initial position and the front of the sphere. The final non-dimensional form of the axial pressure gradient induced by a sphere is:

$$z = \frac{\nu t}{u_0}, \tag{A.24}$$

$$R = \frac{\nu I}{u_0}, \tag{A.25}$$

$$K = \frac{\nu H}{u_0}, \tag{A.26}$$

$$\frac{1}{\rho}\frac{\partial p_\mathrm{ext}}{\partial t} = 3u_0^2\left[\frac{I^3}{(t-H)^4} + \frac{I^6}{(t-H)^7}\right]. \tag{A.27}$$

Appendix B

Coordinate Transformations

Figure B.1 shows the two coordinate systems being used in the spherical pressure field. As previously discussed in Appendix A, the coordinate transform from spherical, (κ, α, β), coordinates to cylindrical, (R, Θ, Z), coordinates is fairly simple. Due to the reliance on the purely axial gradients, with no variation in the radial direction the following assumptions were made:

$$\alpha = 0, \tag{B.1}$$

$$\beta = 0, \tag{B.2}$$

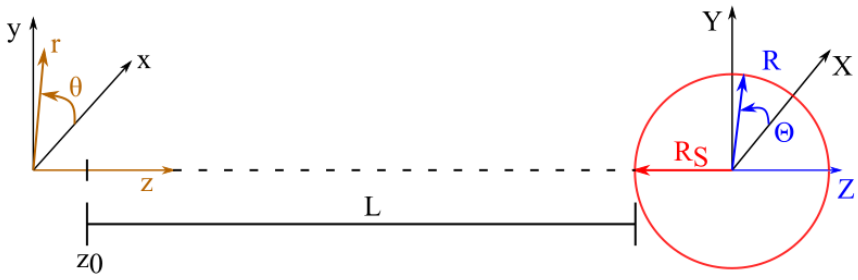

Figure B.1: Transformation of local, sphere coordinate system (R, Θ, Z) to the global, vortex coordinate system (r, θ, z).

which allows for the κ-direction to project onto the negative Z-direction, or

$$\kappa = -Z. \tag{B.3}$$

The final coordinate transformation becomes:

$$K = z_0 + L + R_{\mathrm{S}}, \tag{B.4}$$

$$Z = z + K, \qquad \mathrm{dZ} = \mathrm{dz}, \tag{B.5}$$

$$R = r, \tag{B.6}$$

$$\Theta = \theta. \tag{B.7}$$

Biography

Tanya Johnson graduated from Saucon Valley High School in 2011 before attending the University of Hartford where she earned a B.S. in Mechanical Engineering in 2015. While attending the University of Hartford she was a teaching assistant for physics and engineering courses, performed research as a Dorothy Goodwin Academic Scholar, and was an undergraduate Research Assistant at Georgia Tech through a program sponsored by the NSF. During the summers of 2016 and 2017 she participated in the AFOSR's Air Force Research lab Summer Faculty Fellowship Program at Wright-Patterson Air Force Base. Her research has been presented at the 2017 AFOSR Mid-Atlantic Student Research Day and at the 70th annual meeting of the American Physical Society Division of Fluid Dynamics. She is currently a Ph.D. student at Lehigh University.